Applied Surface Science 409 (2017) 261–269

Contents lists available at ScienceDirect

Applied Surface Science

journal homepage: www.elsevier.com/locate/apsusc

Full Length Article

Microwave plasma-assisted chemical vapor deposition of porous carbon film as supercapacitive electrodes

Ai-Min Wu[a,*], Chen-Chen Feng[a], Hao Huang[a,*], Ramon Alberto Paredes Camacho[a], Song Gao[a], Ming-Kai Lei[a], Guo-Zhong Cao[a,b]

[a] Key Laboratory of Materials Modification by Laser, Ion and Electron Beams (Ministry of Education), School of Materials Science and Engineering, Dalian University of Technology, Dalian 116024, China
[b] Department of Materials Science and Engineering, University of Washington, Seattle, WA 98195, USA

ARTICLE INFO

Article history:
Received 17 December 2016
Received in revised form 27 February 2017
Accepted 1 March 2017
Available online 4 March 2017

Keywords:
Porous carbon film
Double-layer supercapacitor
Microwave plasma
Chemical vapor deposition
Supercapacitive energy storage

ABSTRACT

Highly porous carbon film (PCF) coated on nickel foam was prepared successfully by microwave plasma-assisted chemical vapor deposition (MPCVD) with C_2H_2 as carbon source and Ar as discharge gas. The PCF is uniform and dense with 3D-crosslinked nanoscale network structure possessing high degree of graphitization. When used as the electrode material in an electrochemical supercapacitor, the PCF samples verify their advantageous electrical conductivity, ion contact and electrochemical stability. The test results show that the sample prepared under 1000 W microwave power has good electrochemical performance. It displays the specific capacitance of 62.75 F/g at the current density of 2.0 A/g and retains 95% of its capacitance after 10,000 cycles at the current density of 2.0 A/g. Besides, its near-rectangular shape of the cyclic voltammograms (CV) curves exhibits typical character of an electric double-layer capacitor, which owns an enhanced ionic diffusion that can fit the requirements for energy storage applications.

1. Introduction

With the increasing demand for environment-friendly energy storage technology in recent years, electrochemical supercapacitors have received extensive attention with their attractive features including rapid charge/discharge capability, fast charge transfer, long cyclic life (>10^6) and high power density (2000 W/kg) to fill the gaps left by batteries [1]. Such advantages make them the most applicable in high power supply for both stationary and portable devices of digital communication, memory storage, electric cars and personal electronics [2].

The electrode materials are one of the key components determining the performance of supercapacitors and can be categorized mainly into three types: carbon-based materials, transition metal oxides and conductive polymers [3]. Carbon-based materials are the most widely studied serving as the electrode in electrochemical double-layer capacitors due to their excellent electrical conductivity, chemical stability, high specific surface area and low cost. Plenty of carbon materials with various crystallinity and nanostructures have been attempted, such as carbon nanotubes [4], graphene [5], carbon aerogels [6], carbon nanocomposites [7], meso- and macro-porous carbon materials [8] and hierarchical carbon structure [9]. Two major approaches have been proposed to improve the electrochemical performance of these materials: (1) hybridization [10,11] or doping [12,13] on carbon in order to introduce Faradaic pseudo-capacitance; (2) growing carbon film directly on the electric collector for fast charge transportation, that is, forming highly PCF which has been receiving enormous concern in lithium-ion batteries, supercapacitors and fuel cells [14]. The PCF, especially serving in supercapacitors, demonstrates novel advantages including fast current response and high specific gravimetric capacitance [14,15]. However, most of the nanoproducts are prepared in the form of powder, which means they require to be mixed with conductive binders and additives for the fabrication of electrodes. The handicrafts naturally involve the intrinsic deficiency of reduced electroactive materials and a compromised electrical conductivity, hampering the diffusion of ions, therefore diminishing the capacitance and the long-term stability of the composite. Such electrodes, hence, greatly limit the overall performance of the assembled supercapacitors working as high rate units [2].

* Corresponding authors.
E-mail addresses: aimin@dlut.edu.cn (A.-M. Wu), huanghao@dlut.edu.cn (H. Huang).

http://dx.doi.org/10.1016/j.apsusc.2017.03.017
0169-4332/

In the present work, PCF grows directly on the nickel foam by the means of MPCVD that is able to generate wide-range and uniform plasma through high-power microwave source. This way, as stayed before, the use the polymer binder and conductive additives can be prevented, which greatly simplifies the tedious process of conventional electrode preparation and carbonaceous nanoarrays deposited on the conductive substrates can provide larger effective surface area of materials. Our simple synthesis technique has many advantages such as, low temperature conditions, large-scale production and high-quality products, which guarantee its industrial application in the nearest future. Nickel foam was chosen as the substrate because it acts as a 3D network, which owns abundant inter-connected tunnels with large surface area for carbon deposition. In addition, the catalysis nature of Ni is hypothesized to promote the pyrolysis of carbonaceous precursor gas and improve the growth and crystallization of deposited carbon [16,17]. The PCF electrode combines the features of high accessible surface area and hierarchical additive-free porous structure that collectively increases the contact area between the electrolyte and electroactive material. More ions will participate in building the charged layers at the electrode-electrolyte interface, but their diffusion routes are greatly shortened. The electrochemical tests show the significant results of the PCF prepared under the microwave power of 1000 W, which attained the best electrochemical performance. It displays the specific capacitance of 62.75 F/g in 30 wt.% KOH aqueous solution with the current density of 2.0 A/g and 95% of the capacitance retains after 10,000 cycles at the current density of 2.0 A/g. Besides, Good near-rectangular shape of CV curves was obtained with various scan rates ranging from 50 mV/s to 1000 mV/s. Thus, it is visible that galvanostatic and CV curves of the electrodes show their supercapacitive energy storage, which highlights the potential of well-designed PCF for supercapacitor applications.

2. Experimental

2.1. Fabrication of porous carbon films

The MPCVD system (Fig. S1 in Supplementary) uses exactly the same two magnetron of 1.2 kW (continuous mode) to produce 2.45 GHz linear coaxial-coupled microwave. By adjusting the microwave coupling degree and the gas pressure, stable and uniform plasma can be generated in the working chamber. The nickel foam that was used as substrate had the thickness of 1.0 mm, the surface density of 300 g/m^2 and about 17 pores per square centimeter. The foam was cut into rectangular specimens in the size of 1.0 cm × 2.0 cm and then they were immersed into diluted hydrochloric acid for 5 min in order to remove the oxides on the surface. After being cleaned in the deionized water under sonication, the Ni foam was dried in a vacuum oven and its mass was weighed (m_1). The surface of the Ni foam was activated under plasma conditions with Ar:H_2 (2:1 sccm) as the flowing gas, for 10 min. The feed gas was subsequently changed to C_2H_2:Ar (15:1 sccm). During the deposition process, the inner pressure of the chamber was maintained at 35 Pa; the microwave power was set as 800, 1000 and 1200 W, respectively. The deposition time was fixed as 1 h. The flow rate of C_2H_2:Ar and deposition time were optimized by comparing the results of the orthogonal tests which are displayed in Supplementary as the supporting information (Figs. S2–S3 stand for the experiments under the flow rates of C_2H_2:Ar and Figs. S4–S5 for the results depending on deposition time). The mass of the specimen was re-weighed, $_2$ and the mass of active carbon film was calculated by $m = m_2 - m_1$. The obtained specimens are labeled as PCF-800 W, PCF-1000 W and PCF-1200 W respectively.

2.2. Plasma diagnosis

The plasma diagnosis was executed with the floating harmonic probes being set close to the axial center. The copper probe tip had a length and a diameter of 7 mm and 0.4 mm, respectively. A sinusoidal signal of 5 V was applied between the probe tip and the ground. The current was calculated from the measured voltage drop across the current sensing resistor. The Labview program was employed to analyze the harmonics of the current signal and made calculation to give the electron temperature and ion density, as it is explained later on in our work.

2.3. Characterization

The surface morphology of the PCF was observed with the scanning electron microscopy (SEM) of Zeiss Supra 55 VP. High-resolution transmission electron microscopy (HR-TEM) was observed on FEI Tecnai G20 S-type Twin. The test of Fourier-Transform Infrared Spectrometer (FTIR) was conducted in the wavelength range of 500–4000 cm^{-1} on VERTEX 70. Raman spectra were recorded by an inVia spectrometer (England Renishaw) with a laser excitation wavelength of 632.8 nm. The specific surface area was calculated from the Brunauer-Emmett-Teller (BET) plot of the nitrogen adsorption isotherm.

2.4. Electrochemical measurements

The electrochemical measurements were performed on the workstation CHI760e. A standard 3-electrode system was set with the PCF on nickel foam as the working electrode, Ag/AgCl as the reference electrode, a Pt foil as the counter electrode and 30 wt.% KOH solution as the electrolyte. The nickel foam with the deposited PCF, which was cut into rectangular specimens of 1.0 cm × 2.0 cm, was directly used as the electrode after the synthesis, without any other extra procedure, including mixing the conducting additives and binders with the active material to form a paste that ultimately will be deposited on the current collector. The absence of conducting additives and binders is one of the traits of our technique, which clearly simplifies the electrode preparation and boosts the charge transference between the current collector and the carbon electrode. The scanning rate of CV varied at the range of 50–1000 mV/s. Current density range for charge/discharge was set from 2.0 to 10.0 A/g and the potential range was −0.8 to 0.0 V. The specific capacitance of a single electrode can be calculated by the galvanostatic charge-discharge curves according to the formula $C = (\Delta t \times I) / (m \times \Delta\mu)$, where I is the set discharge current, Δt is the discharge time, m is the net mass of the active material of PCF on single electrode and Δu is the voltage drop upon discharge (excluding the IR drop). The energy density (E_g) and power density (P_g) of each electrode were calculated from discharge region (upward direction versus time) of the galvanostatic charge-discharge test following the formula: $E_g = i/4m \int V_d dt$ and $P_g = E_g/\Delta t$, where i is the applied current density, V_d is the potential as a function of discharging time, m is the mass of active materials and Δt is the discharge time (the energy density is divided by 4 because the experiment was conducted on a three-electrode cell). The electrochemical impedance spectroscopy (EIS) measurements were carried out with an excitation signal of 5 mV in the frequency range of 10 mHz–100 kHz.

3. Results and discussion

Fig. 1(a)–(c) is the SEM images showing the typical interconnected structures with random open pores templated from the framework of Ni foam. The close-up cross-section views (in Fig. 1(a')–(c')) clearly show Region I for nickel foam and Region

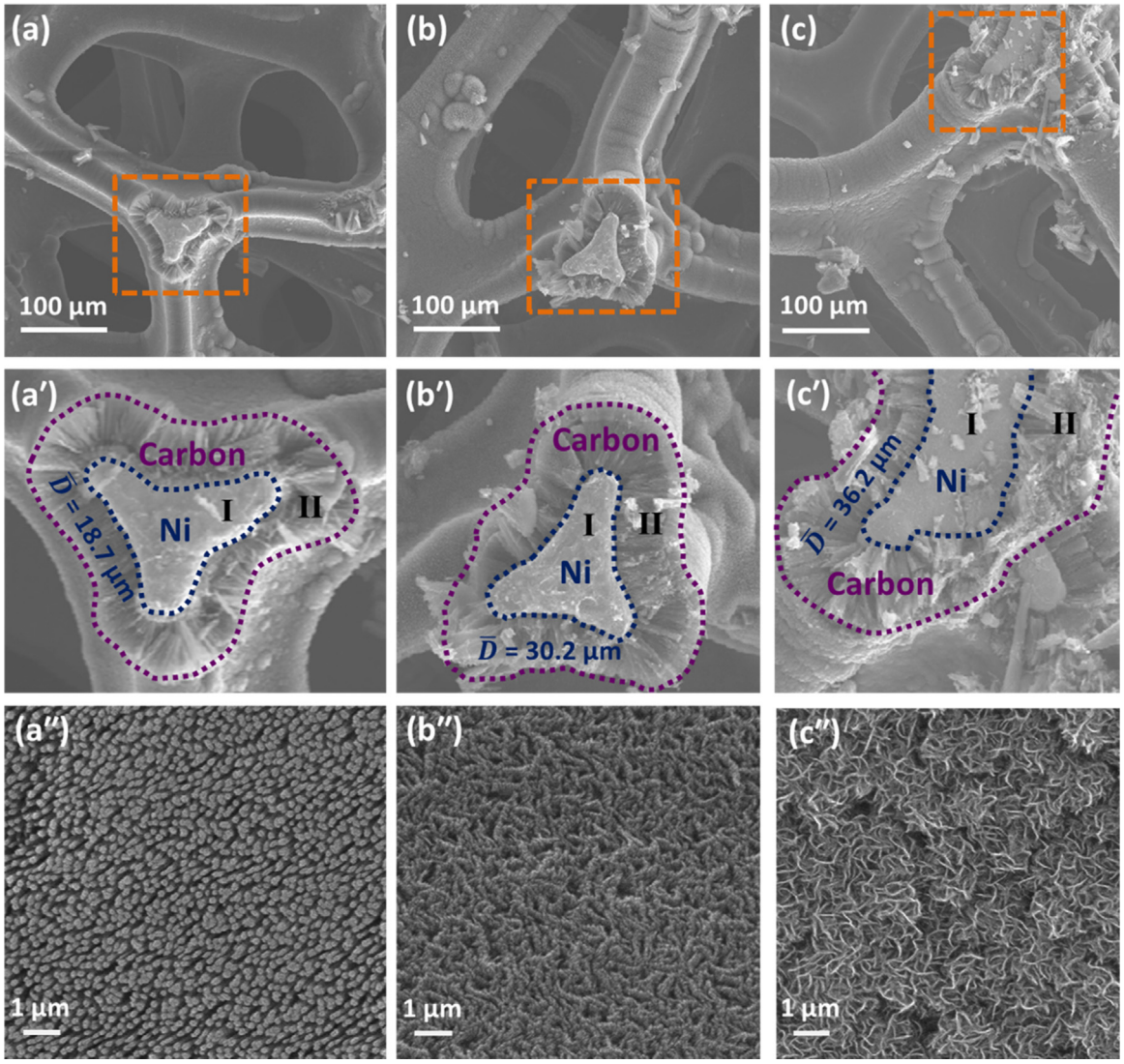

Fig. 1. SEM images of the porous carbon films prepared under the microwave power of (a) 800 W, (b) 1000 W and (c) 1200 W at the magnification of 500×; (a')–(c') The close-up cross-section view of the porous carbon films; (a)–(c) The SEM images of the porous carbon films at the magnification of 20.00 kX.

II for uniformly coated carbon film. The average thickness of the carbon film ($\bar{D}$) increases from 18.7 to 36.2 μm with the increasing microwave power from 800 to 1200 W. Under the resolution of 1 μm, PCF-800 W is found predominantly consisting of homogeneous carbon array with isolated carbon rods (Fig. 1(a)). PCF-1000 W has a wheat-like configuration, which consists of cross-linked carbon stalks with porous structure (Fig. 1(b)). However, the morphology of PCF-1200 W changes into a carbon network and with an obvious reduction of pore volume on the surface (Fig. 1(c)).

Fig. 2(a)–(c) provides the TEM images of the deposited carbon flakes scratched from the surface of PCF-800 W, PCF-1000 W and PCF-1200 W, respectively. PCF-800 W is apparently covered with the carbon clusters as shown in Fig. 2(a). The wrinkle fringe shows the amorphous nature in the close HR-TEM observation (Fig. 2(a')). PCF-1000 W has similar cluster morphology, however with much neat borders shown in Fig. 2(b). The possible explanation could be that the carbon film has been crystallized to onion-like graphite, which clearly exposes its (002) crystal plane with the interplanar spacing of approximate 0.344 nm (Fig. 2(bí)). Notably, the interplanar space is larger than that of single-crystal graphite (0.335 nm), suggesting a possible random combination of graphitic and turbostratic stacking [18]. To further check the degree of graphitization, Raman spectra of PCF-1000 W is employed with the results also shown in Fig. 2(b'). Raman spectrum has two sharp peaks at 1341 and 1595 cm^{-1}, assigning to D and G band, respectively. The D band is caused by structural defects and the partially disordered structure of sp^3 domains. The G band associates with the first-order scattering of the E_{2g} vibrations observed for sp^2 domains [19]. Qualitatively, the peak intensity ratio between the D and G bands (I_D/I_G) is calculated as 2.17, which confirms a large disorder in the microcrystalline carbon [20]. When the microwave power increased to 1200 W, highly aligned multiwall carbon array is deposited as shown in Fig. 2(c'), indicating the unidirectional growth due to the rapid decomposition of acetylene on the Ni surface, which is expected to exert catalytic effect [21].

The plasma generated by the linear coaxial-coupled microwave is monitored with the help of a floating harmonic probe moving from the center (X = 0 cm) to the edge of platform (X = 15 cm) in the typical deposition conditions ($P_{Deposite}$ = 35 Pa; C_2H_2:Ar = 15:1 sccm) at different microwave power of 800, 1000 and 1200 W, respectively, which is shown in Fig. 3(a1). Stable work of the probe is maintained during the entire deposition period up to 1 h. Assuming that the electrons are of Maxwellian distribution, the

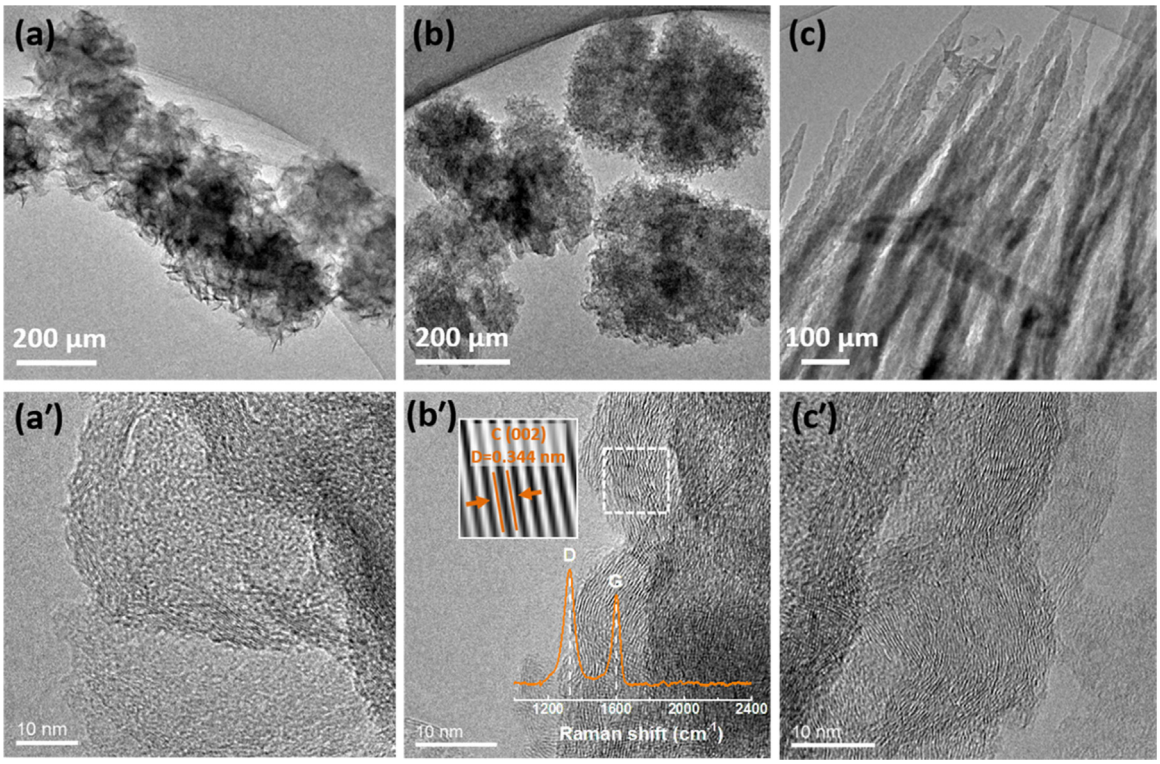

Fig. 2. (a)–(c) TEM images of the porous carbon films prepared under the microwave power of 800, 1000 and 1200 W; (a')–(c') corresponding HR-TEM images of the porous carbon films; Insert in (b') is the Raman spectra of the sample prepared under the microwave power of 1000 W.

probe current i_{pr} can be expanded with modified Bessel functions [22]:

$$i_{pr} = i_i - i_{es}\exp\left[e\left(\bar{V} - V_p\right)/T_e\right] I_0\left(eV_0/T_e\right) - 2i_{es}\exp\left[e\left(\bar{V} - V_p\right)/T_e\right] \sum_{k=1}^{\infty} I_k\left(eV_0/T_e\right)\cos(k\omega t) \quad (1)$$

where V_p is the plasma potential, $\bar{V}$ is the self-bias potential of the probe and i_i and i_{es} are the ion current and electron saturation current, respectively. It should be mentioned that V_0 should be the amplitude of the voltage drop over the probe sheath, so in practice, the voltage drop over R_s was subtracted from the applied bias and the voltage drop over the blocking capacitor was neglected since its capacitance (100 μF in our case) is many orders larger than that of the probe sheath. Assuming that i_i is constant, the electron temperature, T_e and ion density, n_i can be calculated from the equations [23]:

$$|i_{1\omega}|/|i_{2\omega}| = I_1\left(eV_0/T_e\right)/I_2\left(eV_0/T_e\right) \quad (2)$$

$$n_i = |i_{1w}|/2\left(0.61e\mu_B A\right)xI_0\left(eV_0/T_e\right)/I_1\left(eV_0/T_e\right) \quad (3)$$

where μ_B is the Bohm velocity and A is the probe area. During the process of deposition, T_e and n_i were measured by harmonic technique with bias signal V_0 set to 5 V and their values vs. X are plotted in Fig. 3 (a2)–(a4) respectively for the power of 800, 1000 and 1200 W. Fig. 3(a2) displays that T_e (19.18–20.30 eV) and n_i ($5.31–6.83 \times 10^9/cm^3$) shows no major change with the probe moving at 800 W microwave power, which means that the plasma is homogeneously distributed. When the microwave is powered up to 1000 W, T_e (18.67–20.02 eV) decreases insignificantly and n_i ($5.93–8.40 \times 10^9/cm^3$) improves substantially, as shown in Fig. 3(a3). T_e (17.86–19.68 eV) continues to reduce at the power of 1200 W and n_i ($6.68–8.59 \times 10^9/cm^3$) was slightly enhanced (Fig. 3(a4)). Overall, the electron temperature has the decreasing tendency with the increasing microwave power, which is caused by the multistep ionization effect. The enhanced ion density with the microwave power is brought up by the promoted plasma energy that will greatly affect the excitation or ionization degree of the reaction gas [24]. According to above measurements, we find that the values of T_e and n_i are stable and sufficiently high at X = 4 cm, so samples are settled at X = 4 cm at the midline of the platform (Y = 0 cm) during the MPCVD process.

The deposited films were characterized by FTIR spectroscopy with the results shown in Fig. 3(b2)–(b4). All of the as-prepared samples show almost identical peaks, which are typical for the carbon film deposited from hydrocarbon precursors by plasma-enhanced CVD [25]. The peaks display clearly at 3600–3681, 3281–3400, 2893–2925, 2350, 1562–1575 and 875 cm^{-1}, corresponding to —OH, C(sp)-H, C(sp^3)-H_2, C—H (on the benzene ring), C═C and C(sp^2)-H, respectively. The —OH radicals rise due to either the strongly acquainted water particle or from the environment [26]. From Fig. 3(b2)–(b4), it seems that the O—H absorption band for PCF-1000 W was strongest, which means PCF-1000 W has the strongest absorbability and affinity to the water molecule. It is known that the fine hydrophilicity is an important factor for the supercapacitor in aqueous media, influencing the wettability of the electrode surface [27]. Thus, a tentative inference on these results is that PCF-1000 W sample could attain superior electrochemical performance in comparison to PCF-800 W and PCF-1200 W samples respectively. The asymmetric stretching vibration peaks of C(sp)-H, C(sp^2)-H and C(sp^3)-H_2 are attributed to the dissociation (Eqs. (4)–(6)) and ionization (Eqs. (7)–(10)) of C_2H_2. These radicals intrinsically present hydrogen impurity incorporated into the carbonaceous film during its growth. In general, the larger or stronger the C—H absorption band displays, the more impurity the film has [25]. The peak of C—H on the benzene ring is due to the highly reactive C_2H radicals that take part in the polymerization of C_2H_2 molecules into the long-chained C_4H_4 (Eq. (13)). The aromatic ring

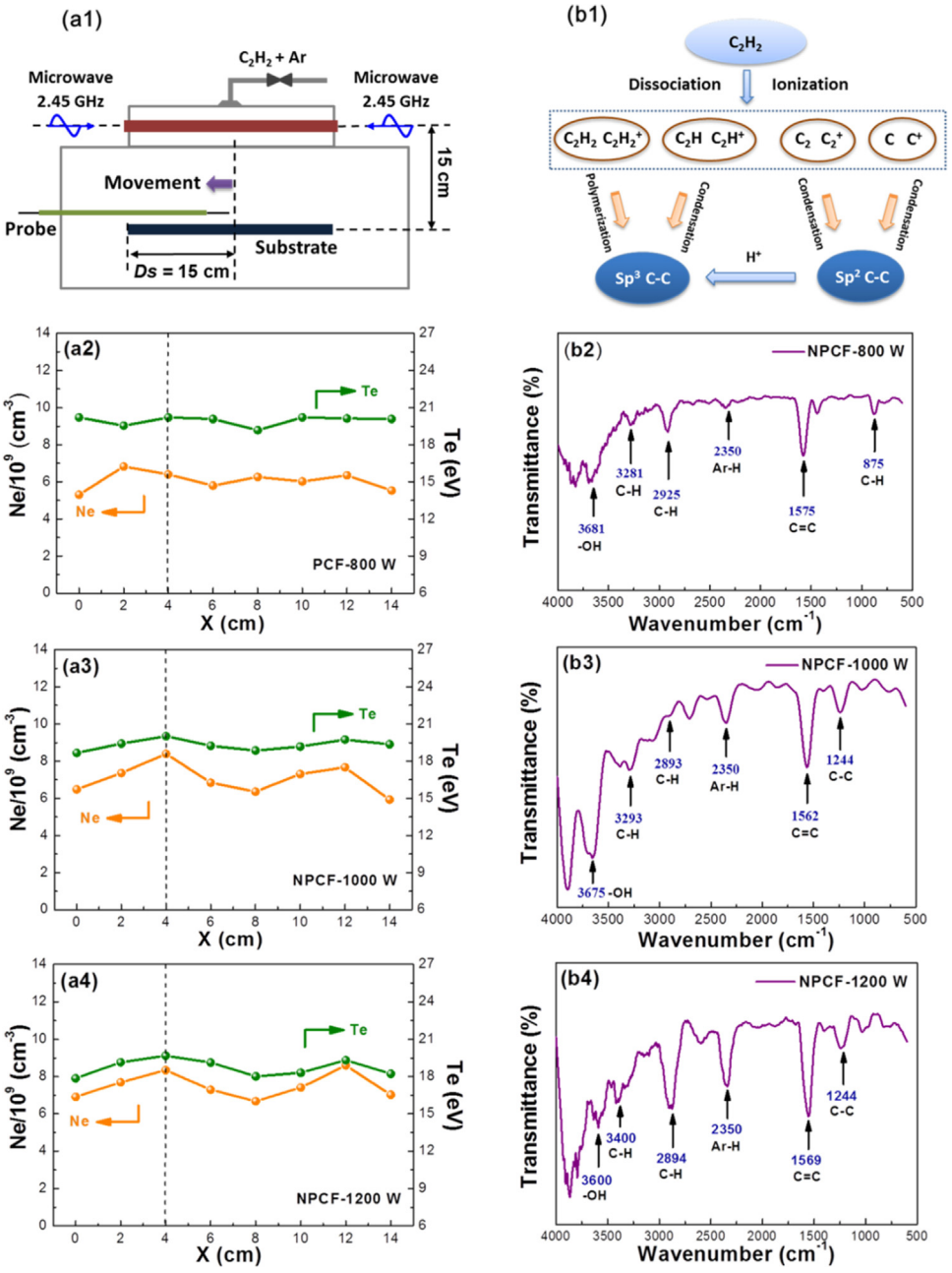

Fig. 3. (a1) Schematic graph of the harmonic electronic probe in sedimentary chamber; (a2)–(a4) the plots of the electron temperature T_e and ion density n_i, measured under the microwave power of 800, 1000 and 1200 W; (b1) schematic graph of gas-phase reactions of C_2H_2 in the process of MPCVD; (b2)–(b4) FTIR spectra of the samples prepared under the microwave power of 800, 1000 and 1200 W.

of benzene are formed by the successive addition reaction of C_2H_2 on vinylacetylene, as in Eq. (14). The strong characteristic peaks at around 1570 cm^{-1} is due to the stretching vibration of carbon nanotube backbone C=C bond, which is cross-linked by removing hydrogen from various hydrocarbon chains [28].

(i) Dissociation and Ionization:

$$C_2H_2 + e^- \rightarrow C_2H + H + e^-(E_T = 7.5\,eV) \quad (4)$$

$$C_2H_2 + e^- \rightarrow C_2H_2^+ + 2e^-(E_T = 11.4eV) \quad (5)$$

$$C_2H_2 + e^- \rightarrow C_2H^+ + H + 2e^-(E_T = 16.5\,eV) \quad (6)$$

$$C_2H_2 + e^- \rightarrow C_2^+ + H_2 + 2e^-(E_T = 17.5eV) \quad (7)$$

$$C_2H_2 + e^- \rightarrow H^+ + C_2H + 2e^-(E_T = 18.4\,eV) \quad (8)$$

$$C_2H_2 + e^- \rightarrow C^+ + CH_2 + 2e^-(E_T = 20.3\,eV) \quad (9)$$

(ii) Condensation:

$$C_2H_2 + C_2H \leftrightarrow C_4H_3 \quad (10)$$

$$C_2H + H \leftrightarrow H_2 + C_2 \quad (11)$$

(iii) Polymerization:

$$2C_2H_2 \leftrightarrow C_4H_4 \quad (12)$$

$$C_2H_2 + C_4H_4 \leftrightarrow C_6H_6 \quad (13)$$

Because the energetic thresholds (E_T) of the above reactions are commonly lower than for the exerted plasma energy T_e, different types of ionized species, such as $C_2H_2^+$, C_2H^+, C^+ and H^+ can be generated together with the neutral radicals, i.e. C_2H and CH [29]. The dehydrogenation of the hydrocarbon structures produces carbon atoms on Ni surface with the encouragement of Ni catalysis [17].

Neutral C atoms continuously arrive at the film surface and form mainly sp^2 coordinated bonds with the surface C atoms, eventually leading to carbon pentagons and other rings [28]. The ionized species with two or more C atoms such as $C_2H_2^+$ mainly contribute to the formation of sp^3 C—C [30] (Fig. 3(b1)). By comparing the samples, the intensity of the C(sp)-H stretching vibration peaks at 3300–3400 cm^{-1} is almost unchanged. The peak of C—H on the benzene ring gradually enhanced with the increase of microwave power, indicating more aromatic rings generated during the successive polymerization reactions of C_2H_2. The C(sp^2)-H peak at 875 cm^{-1} in PCF-800 W disappear with the power improvement, however followed by the birth of mixed sp^2/sp^3 C—C bond instead in PCF-1000 W and PCF-1200 W at about 1244 cm^{-1}. The increasing C—C bonds give rise to the film density as well as the hardness [30]. Meanwhile, we can find gradually intensified stretching vibration peak of C=C bond due to the dehydrogenation reaction and producing large-area crystallized carbon network [28].

The electrochemical properties and device performance of the PCF as electrodes in supercapacitors were studied by the means of CV, galvanostatic charge-discharge and cyclic stability. Fig. 4(a)–(c) represents the CV curves with various scan rates ranging from 50 to 1000 mV/s in the potential range between −0.8 and 0.0 V. The samples present near rectangular and symmetric voltammogram plots with slight distortions, demonstrating small value of time constant (τ) that is proportional to the electrode resistance (R) at a fixed capacitance when voltage transforms. In other words, smaller τ means smaller R which allows quick diffusion and transfer of electrolyte ions within the macro- or meso-pore channels [31]. Furthermore, the distortion of CV curves is inconspicuous even at high scanning rate of 1000 mV/s, implying that the system of electrodes has low contact resistance and good rate capability.

Fig. 4(a')–(c') shows the galvanostatic charge-discharge curves with the current density ranging from 2.0 to 10.0 A/g in the potential range between −0.8 and 0.0 V (the specific capacitance of the electrodes are listed in Table S2 in Supplementary). According to the galvanostatic charge and discharge curves, the highest specific capacitances of 19.50, 62.75 and 41.25 F/g were obtained at a current density of 2.0 A/g corresponding to samples PCF-800 W, PCF-1000 W and PCF-1200 W, respectively. The specific capacitance decreases slightly when the current density rises from 2.0 to 10.0 A/g. Even at the current density of 10.0 A/g, PCF-1000 W still retains specific capacitance of 42.50 F/g, displaying excellent rate of charging and discharging. Fig. 4(d) depicts the significantly larger capacity charge of PCF-1000 W electrode in comparison with the other samples, which is confirmed by its considerably longer discharge time.

When galvanostatic charge-discharge is performed, if the capacitance C is constant, the change of potential with time, $d\varphi/dt$, will be linear relationship with the current i, i.e., $i = Cd\varphi/dt$, which leads to a symmetrical charge-discharge curve. However, in practice the majority of discharge branches are slightly bent, which is generated by the internal resistance (always present in supercapacitors), causing a deviation of linearity. Another reason for the distortion of the discharge curve is the presence of pseudocapacitive reactions during the discharge process. These reactions are produced by the large volume of oxygenated groups on the surface of the carbon electrodes, which can be quickly charged and discharged, contributing with an additional pseudocapacitance [27,32]. Regardless of this behavior, there was no voltage drop at the beginning of the discharge process, indicating a low equivalent series resistance of the PCF [33].

In addition, N_2 adsorption-desorption measurement was carried out in order to furtherly investigate the texture and calculate the specific surface area of PCF specimens using Brunauer–Emmett–Teller technique. PCF-800 W, PCF-1000 W and PCF-1200 W display BET specific surface areas of 241.20, 212.08 and 173.84 $m^2\,g^{-1}$, respectively, with a total pore volume of 0.068, 0.074, and 0.039 $cm^3\,g^{-1}$. The high specific surface and optimized pore structure are beneficial for the enhancement of supercapacitor's electrochemical performance, which is reflected in its capacitance, cycling stability and rate capability. Thus, based on its BET surface area, the surface area normalized capacitance of PCF-1000 W is calculated accordingly as 29.59 $\mu F/cm^2$ at 2.0 A/g. Our result is superior to the capacitive performance of the composite film (20 $\mu F/cm^2$) [34], the porous carbon nanosheets (8.8–6.1 $\mu F/cm^2$) [35], and the activated carbon (about 5 $\mu F/cm^2$) [36,37]. This demonstrates that our study could be an alternative for the synthesis of carbon-based electrode materials for energy storage.

Nevertheless, one unexpected finding should be mentioned, which is the non-monotonic increasing of the capacitance with the microwave power. The capacitance of the PCF varies from 19.50 up to 62.75 F/g when the microwave power is elevated from 800 to 1000 W. However, it decreases to 41.25 F/g as the power reaches 1200 W. This was corroborated before with the findings of the FTIR spectra, where the PCF-1000 W sample owned the largest amount of oxygenated species, which directly enhanced the wettability of the carbon surface and gave rise to its pseudocapacitive behavior. More evidence to explain such behavior of the PCF will be presented later on with the performance of the electrochemical impedance spectroscopy (EIS).

In order to investigate the long-term cycling stability, the specific capacitance of PCF-1000 W as a function of cycle number was conducted at a current density of 2.0 A/g (Fig. 4(e)). The first 20 cycles are to activate electrode materials, which could be considered as the full penetration of the electrolyte within the carbonaceous pores. Up to this point, relatively stable specific capacitance values are obtained. After 10,000 cycles, an outstanding capacitance retention of 95% is attained, demonstrating superior cycling stability that provide favorable prospects for its application as electrode materials for supercapacitors. This suggests that the carbon nanoporous configuration of PCF in the electrodes are well preserved and the onion-like graphite structures are still strongly adhered to the nickel foam, highlighting the advantages of our deposition method.

Energy density (E_g) and power density (P_g) as important parameters, should be considered synthetically for practical applications. By calculation from the galvanostatic charge-discharge, PCF-1000 W has novel E_g that ranges from 1.24 Wh/kg (10.0 A/g) to 1.97 Wh/kg (2.0 A/g), The P_g of the PCF-1000 W electrode can reach 0.28 kW/kg (2.0 A/g) and 1.31 kW/kg (10.0 A/g). The E_g of the PCF-1000 W is higher than those of PCF-800 W and PCF-1200 W and the P_g of the PCF-1000 W is not much different from PCF-800 W and PCF-1200 W as shown in Fig. 4(f). The good electrochemical performance of the PCF electrode is attributed to the positive synergistic effects between the graphitic structure and the conductive nickel foam.

The Nyquist plots for the PCF electrodes are shown in Fig. 5. At high frequency area (close to 100 kHz), the intercept with Z' axis (real impedance axis) represents the intrinsic ohmic resistance of the internal resistance or equivalent series resistance of the electrode material and electrolyte [38]. The internal resistance of PCF-800 W, PCF-1000 W and PCF-1200 W-Ni foam electrodes are 0.25, 0.24 and 0.21 Ω (100 kHz), respectively, shown in the insert of Fig. 5. The increase of the microwave power of PCF enhanced its

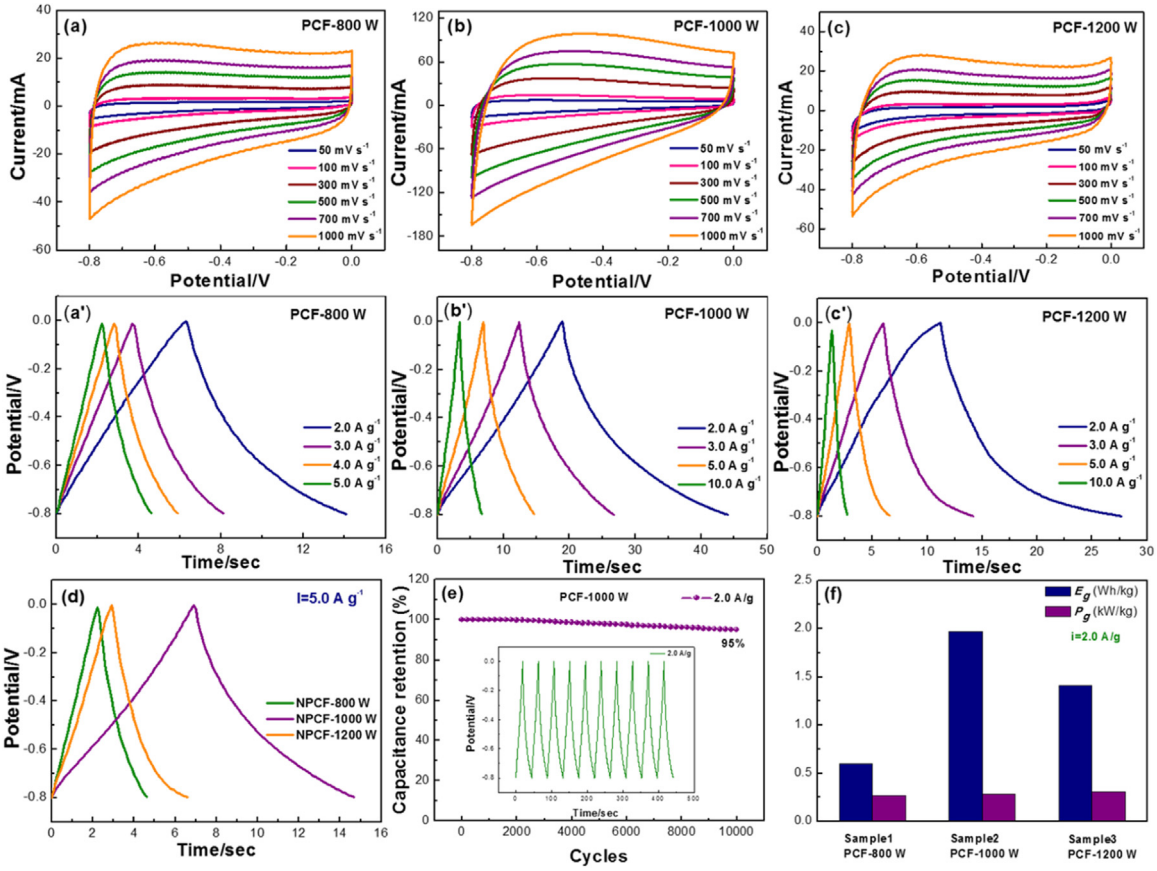

Fig. 4. (a)–(c) CV curves, scanning at different rates in 30 wt.% KOH aqueous electrolyte, of the porous carbon films electrode prepared under the microwave power of 800, 1000 and 1200 W; (a')–(c') galvanostatic charge-discharge curves at different current densities of the porous carbon films electrode; (d) the galvanostatic charge-discharge curves of the porous carbon films at the same current density 5.0 A/g; (e) evaluation of the specific capacitance versus the number of cycles at a constant current density of 2.0 A/g for the porous carbon films electrode prepared under the microwave power of 1000 W, where the inset shows the galvanostatic charge/discharge curves at 2.0 A/g; (f) energy density (E_g) and power density (P_g) of the porous carbon films electrode prepared under the microwave power of 800 W, 1000 W and 1200 W calculated from the galvanostatic charge-discharge profiles at the current density of 2.0 A/g.

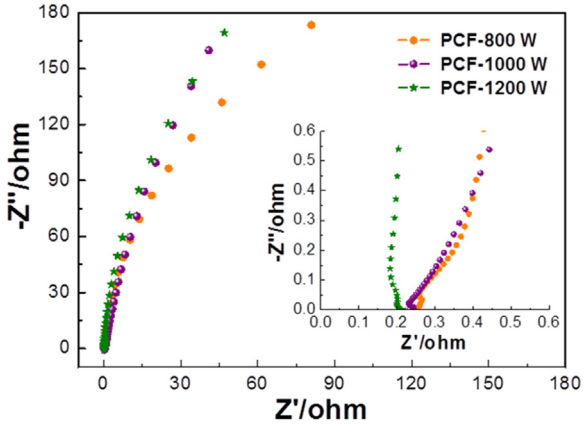

Fig. 5. Nyquist plots of the porous carbon films under the different microwave power of 800, 1000 and 1200 W, respectively; the insert is the close-up image in the high frequency range.

conductivity by promoting the crystalline degree of the deposited carbon. Our resistances are much smaller than the values reported before in other works like functional graphene-Ni foam (0.57 Ω, 100 kHz) [39] and the electrodeposited graphene-Ni foam (0.8 Ω, 100 kHz) [40]. This clearly indicates that the direct contact between PCF and the current collector without any polymer binder is an important feature that helps to decrease the internal resistance of the porous carbon electrode. Thus, charge transfer would be improved during its flowing from and to the nanoporous electrode and the electric collector [41].

At low frequency range, as we know, the linear plot symbolizes the Warburg impedance and the slope of the line reflects the diffusive resistivity of the electrolyte ions within the pores [42]. The slope for PCF-1000 W is larger than those of other samples, unveiling the inherent capacitive nature of the porous carbon electrode and its faster ion diffusion rate (due to a more conductive carbonaceous structure and shorter pathways), which is closer to the characteristic behavior of an ideal capacitor [43]. This behavior directly agrees with the CV and galvanostatic findings. Consequently, according to electrochemical characterization and electrochemical impedance spectroscopy results, the large deal of oxygenated species on the surface, vast nanopores within the carbon film and its high crystalline degree, significantly facilitate the charge storage and ionic transportation of the PCF-1000 W electrode [44].

4. Conclusions

The 3D-crosslinked PCF was grown directly on nickel foam by the MPCVD method. The condensed film was well-crystallized and owned a distinct porous configuration. The PCF prepared under 1000 W microwave power demonstrated ideal electric double-layer capacitive behavior and quick charging/discharging performance due to the following contributions: (i) the interconnected macropores of the Ni form that accelerate kinetic process

of ion diffusion inside of the electrodes; (ii) the large deal of oxygenated groups on the surface which provides additional pseudocapacitance as well as enhanced wettability of the electrode; (iii) well-crystallized carbon structure with remarkable conductivity, which is able to realize a rapid charging/discharging, especially, when the electrode is prepared by in-situ carbon growth and without participation of conductive agents or adhesives. In all, the highlighted achievements of the PCF including facile synthetic route, large-scale production and supercapacitive performance encourage our earnest expectation of its industrial application in the nearest future.

Acknowledgements

The authors gratefully acknowledge the support from the National Key Research and Development Program of China (No. 2016YFB0101206), the Science and Technology Supported Plan (Industry Field) of Changzhou (CE20160022), the Project of Innovative Talents Introduction and Training of Changzhou (CQ20153002), National Torch Program (No. 2014GH580515), the Fundamental Research Funds for the Central Universities (DUT16LAB03, DUT15LAB05).

Appendix A. Supplementary data

Supplementary data associated with this article can be found, in the online version, at http://dx.doi.org/10.1016/j.apsusc.2017.03.017.

References

[1] Z.-S. Wu, A. Winter, L. Chen, Y. Sun, A. Turchanin, X. Feng, K. Müllen, Three-dimensional nitrogen and boron co-doped graphene for high-performance all-solid-state supercapacitors, Adv. Mater. 24 (2012) 5130–5135, http://dx.doi.org/10.1002/adma.201201948.
[2] J. Yan, Q. Wang, T. Wei, Z. Fan, Recent advances in design and fabrication of electrochemical supercapacitors with high energy densities, Adv. Energy Mater. 4 (2014) 1300816, http://dx.doi.org/10.1002/aenm.201300816.
[3] S. He, H. Hou, W. Chen, 3D porous and ultralight carbon hybrid nanostructure fabricated from carbon foam covered by monolayer of nitrogen-doped carbon nanotubes for high performance supercapacitors, J. Power Sources 280 (2015) 678–686, http://dx.doi.org/10.1016/j.jpowsour.2015.01.159.
[4] S. Gao, K. Wang, Z. Du, Y. Wang, A. Yuan, W. Lu, L. Chen, High power density electric double-layer capacitor based on a porous multi-walled carbon nanotube microsphere as a local electrolyte micro-reservoir, Carbon 92 (2015) 254–261, http://dx.doi.org/10.1016/j.carbon.2015.04.034.
[5] Y.-Y. Peng, Y.-M. Liu, J.-K. Chang, C.-H. Wu, M.-D. Ger, N.-W. Pu, C.-L. Chang, A facile approach to produce holey graphene and its application in supercapacitors, Carbon 81 (2015) 347–356, http://dx.doi.org/10.1016/j.carbon.2014.09.067.
[6] Y. Ren, Q. Xu, J. Zhang, H. Yang, B. Wang, D. Yang, J. Hu, Z. Liu, Functionalization of biomass carbonaceous aerogels: selective preparation of MnO_2@CA composites for supercapacitors, ACS Appl. Mater. Interfaces 6 (2014) 9689–9697, http://dx.doi.org/10.1021/am502035g.
[7] D.T. Pham, T.H. Lee, D.H. Luong, F. Yao, A. Ghosh, V.T. Le, Carbon nanotube-bridged graphene 3D building blocks for ultrafast compact supercapacitors, ACS Nano (2015) 2018–2027.
[8] S. Tanaka, H. Fujimoto, J.F.M. Denayer, M. Miyamoto, Y. Oumi, Y. Miyake, Surface modification of soft-templated ordered mesoporous carbon for electrochemical supercapacitors, Microporous Mesoporous Mater. 217 (2015) 141–149, http://dx.doi.org/10.1016/j.micromeso.2015.06.017.
[9] Y. Zhao, W. Ran, J. He, Y. Song, C. Zhang, D.-B. Xiong, F. Gao, J. Wu, Y. Xia, Oxygen-rich hierarchical porous carbon derived from artemia cyst shells with superior electrochemical performance, ACS Appl. Mater. Interfaces 7 (2015) 1132–1139, http://dx.doi.org/10.1021/am506815f.
[10] X. Wang, X. Fan, G. Li, M. Li, X. Xiao, A. Yu, Z. Chen, Composites of MnO_2 nanocrystals and partially graphitized hierarchically porous carbon spheres with improved rate capability for high-performance supercapacitors, Carbon 93 (2015) 258–265, http://dx.doi.org/10.1016/j.carbon.2015.05.072.
[11] E. Wilson, M.F. Islam, Ultracompressible, high-rate supercapacitors from graphene-coated carbon nanotube aerogels, ACS Appl. Mater. Interfaces 7 (2015) 5612–5618, http://dx.doi.org/10.1021/acsami.5b01384.
[12] A. Chen, Y. Yu, T. Xing, R. Wang, Y. Li, Y. Li, Synthesis of nitrogen-doped hierarchical porous carbon for supercapacitors, Mater. Lett. 157 (2015) 30–33, http://dx.doi.org/10.1016/j.matlet.2015.05.082.
[13] J. Han, L.L. Zhang, S. Lee, J. Oh, K.-S. Lee, J.R. Potts, J. Ji, X. Zhao, R.S. Ruoff, S. Park, Generation of B-doped graphene nanoplatelets using a solution process and their supercapacitor applications, ACS Nano 7 (2013) 19–26, http://dx.doi.org/10.1021/nn3034309.
[14] J. Chmiola, C. Largeot, P.-L. Taberna, P. Simon, Y. Gogotsi, Monolithic carbide-derived carbon films for micro-supercapacitors, Science 328 (2010).
[15] M. Kaempgen, C.K. Chan, J. Ma, Y. Cui, G. Gruner, Printable thin film supercapacitors using single-walled carbon nanotubes, Nano Lett. 9 (2009) 1872–1876, http://dx.doi.org/10.1021/nl8038579.
[16] N. Jeong, S.O. Han, H. Kim, H. Kim, Y. You, Growth of multi-walled carbon nanotubes by catalytic decomposition of acetylene on Ni-supported carbon fibers prepared by the heat-treatment of cellulose fibers, J. Mater. Sci. 46 (2011) 2041–2049, http://dx.doi.org/10.1007/s10853-010-5036-9.
[17] W.J. Lee, S.S.A. Syed-Hassan, C.-Z. Li, Formation of carbon on non-porous Ni mesh during the catalytic pyrolysis of acetylene, Fuel Process. Technol. 104 (2012) 319–324, http://dx.doi.org/10.1016/j.fuproc.2012.06.002.
[18] M. Sevilla, A.B. Fuertes, Fabrication of porous carbon monoliths with a graphitic framework, Carbon 56 (2013) 155–166, http://dx.doi.org/10.1016/j.carbon.2012.12.090.
[19] S. Hu, K. Evans, D. Craw, K. Rempel, J. Bourdet, J. Dick, K. Grice, Raman characterization of carbonaceous material in the Macraes orogenic gold deposit and metasedimentary host rocks, New Zealand, Ore Geol. Rev. 70 (2015) 80–95, http://dx.doi.org/10.1016/j.oregeorev.2015.03.021.
[20] W. Lee, J.H. Moon, Monodispersed N-doped carbon nanospheres for supercapacitor application, ACS Appl. Mater. Interfaces 6 (2014) 13968–13976, http://dx.doi.org/10.1021/am5033378.
[21] B. Lu, H. Huang, X.L. Dong, J.P. Lei, Catalytic pyrogenation synthesis of C/Ni composite nanoparticles: controllable carbon structures and high permittivities, J. Phys. D: Appl. Phys. 43 (2010) 105403, http://dx.doi.org/10.1088/0022-3727/43/10/105403.
[22] J. Pang, W. Lu, Y. Xin, H. Wang, J. He, J. Xu, Plasma diagnosis for microwave ECR plasma enhanced sputtering deposition of DLC films, Plasma Sci. Technol. 14 (2012) 172–176, http://dx.doi.org/10.1088/1009-0630/14/2/17.
[23] M.-H. Lee, S.-H. Jang, C.-W. Chung, Floating probe for electron temperature and ion density measurement applicable to processing plasmas, J. Appl. Phys. 101 (2007) 33305, http://dx.doi.org/10.1063/1.2204352.
[24] R. Goswami, T. Jana, S. Ray, Transparent polymer and diamond-like hydrogenated amorphous carbon thin films by PECVD technique, J. Phys. D: Appl. Phys. 41 (2008) 155413, http://dx.doi.org/10.1088/0022-3727/41/15/155413.
[25] C.J. Tang, A.J.S. Fernandes, X.F. Jiang, J.L. Pinto, H. Ye, Effect of methane concentration in hydrogen plasma on hydrogen impurity incorporation in thick large-grained polycrystalline diamond films, J. Cryst. Growth 426 (2015) 221–227, http://dx.doi.org/10.1016/j.jcrysgro.2015.06.018.
[26] P. Nithyadharseni, M.V. Reddy, B. Nalini, T.R. Ravindran, B.C. Pillai, M. Kalpana, B.V.R. Chowdari, Electrochemical studies of CNT/Si–SnSb nanoparticles for lithium ion batteries, Mater. Res. Bull. 70 (2015) 478–485, http://dx.doi.org/10.1016/j.materresbull.2015.05.019.
[27] E. Frackowiak, Carbon materials for supercapacitor application, Phys. Chem. Chem. Phys. 9 (2007) 1774–1785, http://dx.doi.org/10.1039/b618139m.
[28] Y. Wang, X. Gao, H.-J. Qian, Y. Ohta, X. Wu, G. Eres, K. Morokuma, S. Irle, Quantum chemical simulations reveal acetylene-based growth mechanisms in the chemical vapor deposition synthesis of carbon nanotubes, Carbon 72 (2014) 22–37, http://dx.doi.org/10.1016/j.carbon.2014.01.020.
[29] J. Benedikt, Plasma-chemical reactions: low pressure acetylene plasmas, J. Phys. D: Appl. Phys. 43 (2010) 43001, http://dx.doi.org/10.1088/0022-3727/43/4/043001.
[30] A. Aijaz, K. Sarakinos, M. Raza, J. Jensen, U. Helmersson, Principles for designing sputtering-based strategies for high-rate synthesis of dense and hard hydrogenated amorphous carbon thin films, Diam. Relat. Mater. 44 (2014) 117–122, http://dx.doi.org/10.1016/j.diamond.2014.02.014.
[31] J. Jiang, H. Chen, Z. Wang, L. Bao, Y. Qiang, S. Guan, J. Chen, Nitrogen-doped hierarchical porous carbon microsphere through KOH activation for supercapacitors, J. Colloid Interface Sci. 452 (2015) 54–61, http://dx.doi.org/10.1016/j.jcis.2015.04.012.
[32] A.G. Pandolfo, A.F. Hollenkamp, Carbon properties and their role in supercapacitors, J. Power Sources 157 (2006) 11–27, http://dx.doi.org/10.1016/j.jpowsour.2006.02.065.
[33] Q. Tang, M. Sun, S. Yu, G. Wang, Preparation and supercapacitance performance of manganese oxide nanosheets/graphene/carbon nanotubes ternary composite film, Electrochim. Acta 125 (2014) 488–496, http://dx.doi.org/10.1016/j.electacta.2014.01.139.
[34] X. Li, X. Zang, Z. Li, X. Li, P. Li, P. Sun, X. Lee, R. Zhang, Z. Huang, K. Wang, D. Wu, F. Kang, H. Zhu, Large-area flexible core-shell graphene/porous carbon woven fabric films for fiber supercapacitor electrodes, Adv. Funct. Mater. 23 (2013), http://dx.doi.org/10.1002/adfm.201300464.
[35] X. Wang, Y. Yin, C. Hao, Z. You, A high-performance three-dimensional micro supercapacitor based on ripple-like ruthenium oxide–carbon nanotube composite films, Carbon 82 (2015) 436–445, http://dx.doi.org/10.1016/j.carbon.2014.10.087.
[36] M. Sevilla, A.B. Fuertes, Direct synthesis of highly porous interconnected carbon nanosheets and their application as high-performance supercapacitors, ACS Nano 8 (2014) 5069–5078, http://dx.doi.org/10.1021/nn501124h.
[37] Y.S. Yun, S.Y. Cho, J. Shim, B.H. Kim, S.-J. Chang, S.J. Baek, Y.S. Huh, Y. Tak, Y.W. Park, S. Park, H.-J. Jin, Microporous carbon nanoplates from regenerated silk

proteins for supercapacitors, Adv. Mater. 25 (2013) 1993–1998, http://dx.doi.org/10.1002/adma.201204692.
[38] Y. Liang, F. Liang, H. Zhong, Z. Li, R. Fu, D. Wu, An advanced carbonaceous porous network for high-performance organic electrolyte supercapacitors, J. Mater. Chem. A 1 (2013) 7000, http://dx.doi.org/10.1039/c3ta11051f.
[39] Z. Huang, H. Zhang, Y. Chen, W. Wang, Y. Chen, Y. Zhong, Microwave-assisted synthesis of functionalized graphene on Ni foam as electrodes for supercapacitor application, Electrochim. Acta 108 (2013) 421–428, http://dx.doi.org/10.1016/j.electacta.2013.06.080.
[40] S. Yang, B. Deng, R. Ge, L. Zhang, H. Wang, Z. Zhang, W. Zhu, G. Wang, Electrodeposition of porous graphene networks on nickel foams as supercapacitor electrodes with high capacitance and remarkable cyclic stability, Nanoscale Res. Lett. 9 (2014) 672, http://dx.doi.org/10.1186/1556-276X-9-672.
[41] J.-S. Lee, S.-I. Kim, J.-C. Yoon, J.-H. Jang, Chemical vapor deposition of mesoporous graphene nanoballs for supercapacitor, ACS Nano 7 (2013) 6047–6055, http://dx.doi.org/10.1021/nn401850z.
[42] J. Sun, W. Li, B. Zhang, G. Li, L. Jiang, Z. Chen, R. Zou, J. Hu, 3D core/shell hierarchies of MnOOH ultrathin nanosheets grown on NiO nanosheet arrays for high-performance supercapacitors, Nano Energy 4 (2014) 56–64, http://dx.doi.org/10.1016/j.nanoen.2013.12.006.
[43] S. Devaraj, N. Munichandraiah, Electrochemical supercapacitor studies of nanostructured α-MnO_2 synthesized by microemulsion method and the effect of annealing, J. Electrochem. Soc. 154 (2007) A80, http://dx.doi.org/10.1149/1.2404775.
[44] C. Falco, J.M. Sieben, N. Brun, M. Sevilla, T. van der Mauelen, E. Morallón, D. Cazorla-Amorós, M.-M. Titirici, Hydrothermal carbons from hemicellulose-derived aqueous hydrolysis products as electrode materials for supercapacitors, ChemSusChem 6 (2013) 374–382, http://dx.doi.org/10.1002/cssc.201200817.